Bioorganic Chemistry 39 (2011) 28–41

Contents lists available at ScienceDirect

Bioorganic Chemistry

journal homepage: www.elsevier.com/locate/bioorg

NMR and amber analysis of the neamine pharmacophore for the design of novel aminoglycoside antibiotics

Cenk A. Andac [a,*], Thomas C. Stringfellow [b], Ulfert Hornemann [b], Ningur Noyanalpan [c]

[a] Department of Pharmacology, Medical School, Dicle University, Diyarbakir 21280, Turkiye
[b] School of Pharmacy, University of Wisconsin, Madison, WI 53705, United States
[c] School of Pharmacy, Gazi University, Ankara 06330, Turkiye

ARTICLE INFO

Article history:
Received 18 September 2010
Available online 23 October 2010

Keywords:
Aminoglycoside
Neamine
NMR
AMBER
Molecular dynamics
Clustering
Exchange rate constants
p*Ka*
Transition state analysis
Boltzmann's distribution law

ABSTRACT

The dependence of the solution structure of neamine on pH was determined by NMR and AMBER molecular dynamics methods at pD 3.3, pD 6.5, and pD 7.4 in D_2O at 25 °C. Unlike neamine structures at pD 3.3 and 6.5, which essentially showed only one conformer, slowly exchanging primary, P-state, and secondary, S-state, neamine conformers populated on the NMR time scale at ~80% and ~20%, respectively, were detected at pD 7.4 with kinetic constants $k_{on(P\rightarrow S)} = 1.9771\ s^{-1}$ and $k_{off(S\rightarrow P)} = 1.1319\ s^{-1}$. A tertiary, T-state, neamine species populated at ~3% was also detected by NMR at pD 7.4. The p*Ka* values determined by NMR titration experiments are p*Ka*1 6.44 ± 0.13 for N3 of ring-II, p*Ka*2 7.23 ± 0.09 for N2′ of ring-I, p*Ka*3 7.77 ± 0.19 for N1 of ring-II, and p*Ka*4 8.08 ± 0.15 for N6′ of ring-I. Ring-I and ring-II of the P-state neamine and ring-I of the S and T-states of neamine possess the $^4C_1$ chair conformation between pD 3.3 and pD = 7.4. In contrast, ring-II of the S and T-states of neamine most likely adopt the $^6rH_1$ half-chair conformation. The P and S-states of neamine exhibit a negative syn-ψ glycosidic geometry. The exocyclic aminomethyl group of ring-I adopts the gt exocyclic rotamer conformation around physiological pHs while the gg exocyclic rotamer conformation predominates in acidic solutions near and below pH 4.5. Neamine exists in the P-state as a mixture of tetra-/tri-/di-protonated species between pD 4.5 and pD 7.4, while the S-state neamine exist only in a di-protonated species around physiological pDs. The existence of the S-state neamine may facilitate binding of neamine-like aminoglycosides by favorable entropy of binding to the A-site of 16S ribosomal RNA, suggesting that novel aminoglycoside compounds carrying a S-state neamine pharmacophore can be developed.

1. Introduction

Aminoglycoside antibiotics, such as gentamicin and kanamycin, have long been used as efficient antimicrobial agents active against both gram-positive and gram-negative bacteria as well as mycobacteria [1]. These antibiotics are considered to exert their antimicrobial activity mainly by interacting with bacterial ribosomes at the aminoacyl-tRNA binding site, the A-site, which is constituted by specific nucleotides of 16S ribosomal RNA in the decoding region of their 30S subunits [2]. Antibiotic binding interferes with the fidelity of mRNA translation, results in miscoding, and leads ultimately to bacterial cell death [3]. The aminoglycosides, however, can be toxic to mammalian cells (nephrotoxic and ototoxic in humans) at high doses and are prone to undergo a variety of chemical modifications by different bacterial aminoglycoside antibiotic inactivating enzymes [4,5].

Aminoglycosides bound to bacterial resistance enzymes exhibit different conformations involving rotations around the two bonds that constitute the glycosidic linkage extant between rings I and II in comparison to the glycosidic linkages occurring in aminoglycosides complexed with the A site of 16S rRNA [6,7]. The rotation that is crucially affected in enzyme bound aminoglycosides is characterized by the torsion angles φ(H1′–C1′–O4–C4)/ψ(C1′–O4–C4–H4), Fig. 1, which assume values around −21/152 for neamine- or paromamine-like aminoglycosides in complex with resistance enzymes. This results in an anti-ψ geometry for rings I and II [7,8], where N6′ of ring I and N3 of ring II are anti-axially oriented. In contrast, aminoglycosides in complex with the A site of 16S rRNA adopt a negative syn-ψ geometry, where Φ/ψ is about −40°/−30° [8], where N6′ of ring I and N3 of ring II are syn-axially oriented.

Abbreviations: nea33/65/74, neamine at pD 3.3/6.5/7.4; nea65p/s, the primary/secondary neamine species at pD 6.5; nea74p/s/t, the primary/secondary/tertiary neamine species at pD 7.4; nea-4/3/2H, the tetra-/tri-/di-protonated state of the primary neamine species; nea-2h, the di-protonated state of the secondary neamine species.

* Corresponding author. Fax: +90 412 248 8440.
E-mail address: cenk_andac@yahoo.com (C.A. Andac).

0045-2068/$ - see front matter © 2010 Elsevier Inc. All rights reserved.
doi:10.1016/j.bioorg.2010.10.002

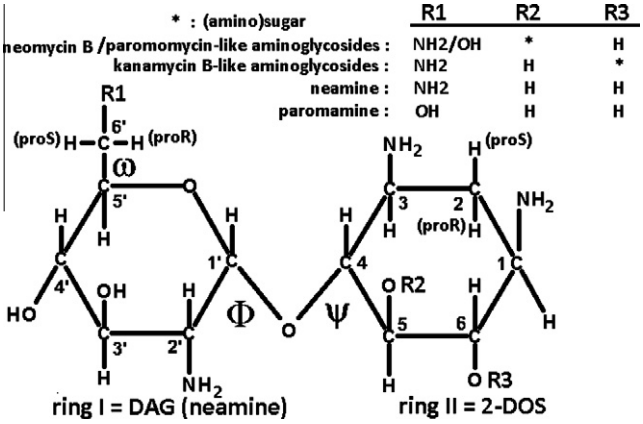

Fig. 1. Haworth formula of neamine-/paromamine-like aminoglycosides showing atom numbering and the torsion angles Φ (H1′–C1′–O–C4), ψ (C1′–O–C4–H4) and ω (H5′–C5′–C6′–N/O6′) for rings I and II. The DAG (2,6-diamino-2,6-dideoxy glucosyl) group is denoted as ring I and the 2-DOS (2-deoxystreptaminyl) group is called ring II.

The increasing concerns about bacterial resistance and toxic effects have led to the development of semisynthetic aminoglycosides which are less toxic and less sensitive to enzymatic modification. Understanding the binding modes of bound aminoglycosides in complex with 16S rRNA [9,10] and bacterial resistance enzymes [7] at the molecular level recently has been a major strategy to develop semisynthetic aminoglycoside analogs. Extensive research and analysis on the binding interactions between RNA and aminoglycosides have proven that neamine, Fig. 1, is the most suitable core structure that possesses antibiotic activity and, therefore, has been commonly applied in the development of synthetic analogs [11,12]. However, the structure of neamine in the unbound state has not been fully explored so far.

Here, the unbound solution structures of neamine at pH 3.3, 6.5 and 7.4 at 25 °C in D_2O are investigated by NMR and computational techniques. p*Ka* values for the amino groups of neamine are determined by H1 NMR titration experiments. Kinetic and NMR properties for the most populated two different neamine species found to exist at near physiological pH values are revealed here, to the best of our knowledge, for the first time in literature. Information gained from the NMR and computational data are then utilized to propose novel aminoglycoside antibiotics.

2. Materials and methods

2.1. Synthesis and characterization of neamine

Several batches of neamine were synthesized by acid hydrolysis of neomycin B as described by Wong et al. [11]. The acid hydrolysis reaction of neomycin B was monitored by TLC using a solvent mixture of BuOH/AcOH/H_2O (2/2/1) and a solution of 1% ninhydrin as an indicator (Rf: 0.32 and 0.37) [11,13]. The acidic precipitate formed at the end of the reaction was filtered off and washed with ether several times to give the desired product (Fig. 1) in salt form (neamine·4HCl) as an off-white powder (yield: 4.45 g, 9.5 mmol, 91%). For NMR samples, the neamine product was further recrystallized twice in fresh methanol and filtered off as white powders, which were then washed with diethyl ether after each crystallization step. The remaining white powders were vacuum-aspirated for 1 day to remove residual methanol, ether and water.

The HPLC-MS (Agilent 1100 HPLC-MSD SL Mass Spectrometer, available in the School of Pharmacy at the University of Wisconsin-Madison, WI USA) characterization of neamine was indirectly implemented on a neamine derivative, 1,2′,3,6′-tetrakis-N-trifluoroacetyl neamine, which was synthesized using the neamine·4HCl product as the starting material according to a chemical procedure described by Hunziker et al. [13] An *m*/*e* ratio of 707.1 Da was found in positive ion mode (M^+) for the neamine derivative (MW = 706.1 Da) by LC–MS. The purity of freshly synthesized neamine batches were confirmed by NMR. ^{1}H NMR (D_2O, δ = 4.8 ppm): 5.82 ppm (d, H), 3.94–3.85 ppm (m, 3H), 3.59 ppm (t, H), 3.51–3.32 ppm (m, 5H), 3.24 ppm (m, H), 3.16 ppm (q, H), 2.4 ppm (m, H), 1.8 ppm (q, H). Proton-coupled ^{13}C (D_2O): 97–95 ppm (d, CH); 78.5–76.8 ppm (d, CH); 76.2–74.5 ppm (d, CH); 73.5–72 ppm (d, CH); 72.8–70 ppm (d, CH); 70–69 ppm (d, CH); 68.6–67.8 ppm (d, CH); 54.5–53.2 ppm (d, CH); 50.8–49.4 ppm (d, CH); 49.3–48 ppm (d, CH); 42–39 ppm (t, CH_2), 29.8–26.5 ppm (t, CH_2).

2.2. Titration analysis and pKa

A micro NMR-pH electrode from Mettler Toledo Analytical, Inc. was used both for potentiometric and NMR titration experiments. 0.5 M NaOD and/or 0.5 M DCl solutions (Aldrich Chemicals) were used to adjust the pD of ~10 mM neamine solutions in D_2O. p*Ka* values for the amino groups of neamine were determined by a line fitting procedure via Origin Software v.6 (http://www.originlab.com), which utilized Eq. (1) [14], by plotting ^{1}H NMR chemical shifts (δ in ppm) for the primary vicinal protons of the neamine amino groups (e.g., H3 for the N3 amino group of ring II) versus pD (from

$$\mathrm{pD} = \mathrm{p}Ka + \log[(\delta_{\mathrm{prot}} - \delta_{\mathrm{obs}})/(\delta_{\mathrm{obs}} - \delta_{\mathrm{deprot}}) \quad (1)$$

3.3 to 8.7). δ_{prot} and δ_{deprot} in Eq. (1) represent upper and lower bounds for the protonated and deprotonated states of the corresponding amino groups, respectively, while δ_{obs} is a chemical shift in between the boundary states.

2.3. NMR analysis

NMR samples were weighted out and dissolved in 0.6 ml of D_2O in Eppendorf tubes to yield a final neamine concentration of ~10 mM. A micro NMR-pH electrode was used to adjust the pD with 0.5 M NaOD and/or 0.5 M DCl solutions (Aldrich Chemicals). O_2 was removed by bubbling N_2 gas through the samples. The air-free NMR samples were transferred to 5 mm NMR tubes, which were then immediately flame-sealed.

400 and 500 MHz Varian Unity INOVA NMR spectrometers (available in the School of Pharmacy at the University of Wisconsin-Madison, WI USA) were used to acquire homunuclear 1D/2D NMR spectra (^{1}H, ^{13}C, gCOSY90, gDQF-COSY, and ^{1}H,^{1}H-NOESY {t_{mix} = 75 ms}) using quad-nucleus NMR probes (the qn4549 probe for the V400 MHz unit and the qn6121 probe for the V500 MHz unit) and indirect NMR data (gHMBC) using a tunable triple-resonance probe (the hcx4765 probe for the V500 MHz unit). All NMR data were obtained at 25 °C in D_2O. FID data were processed by Varian NMR v6.1C and Mestre-C v.1.1,2.3a,3.5.1 (http://mestrelab.com) NMR software packages. All 1D/2D NMR spectra were referenced to the HDO peak at δ = 4.8 ppm.

Anomeric/transglycosidic NOE cross-peaks were integrated on 2D-NOESY spectra and normalized by Mestre-C NMR software to the corresponding inverted diagonal-peaks, H1′ for the primary species and h1′ for the secondary species, whose integral was set to -10^5 integral units (iu).

Dihedral angles for intra-residual vicinal protons were determined by an empirically generalized Karplus-like equation developed for conformationally rigid six-membered ring systems by Haasnoot, De Leeuw and Altona (HLA) [15].

2.4. Determination of conformational exchange rate constants of neamine

Exchange rate constants between the primary (P) and secondary (S) conformers of neamine, generically expressed by Eq. (2), are k_{PS} (=$1/\tau_P$) in Hz for conversion from P to S states and k_{SP} (=$1/\tau_S$) in Hz for conversion from S to P states of neamine, which are inversely related to the time-life of the P (τ_P) and S (τ_S) states, respectively. When the overall exchange is at equilibrium, the exchange constant can be defined as $K_{ex} = k_{PS}/k_{SP}$.

$$P \underset{k_{SP}(=1/\tau_S)}{\overset{k_{PS}(=1/\tau_P)}{\rightleftharpoons}} S \quad (2)$$

At slow exchange rates, k_{PS} and k_{SP} can be determined by Eqs. (3) and (4), respectively,

$$1/T2_S = 1/T2 + k_{PS} \quad (3)$$

$$1/T2_P = 1/T2 + k_{SP} \quad (4)$$

where T 2 is the transverse (spin–spin) relaxation time [1 1 5] in seconds for a spin in fast exchange, which can be determined by Eq. (5) in which $\Delta\nu_{1/2}$ is the line-width in Hz at the half height of the NMR peak at fast exchange. Similarly, T 2_P and T 2_S are the spin–spin relaxation times in seconds for the same spin sampling P and S states at slow exchange rates, which can be computed by Eq. (6) and Eq. (7), respectively, where $\Delta\nu_{1/2(P)}$ and $\Delta\nu_{1/2(S)}$ are the corresponding line-widths at the half height of the peak in P or S states at slow exchange.

$$T2 = 1/\pi\Delta\nu_{1/2} \quad (5)$$

$$T2_P = 1/\pi\Delta\nu_{1/2(P)} \quad (6)$$

$$T2_S = 1/\pi\Delta\nu_{1/2(S)} \quad (7)$$

2.5. Calculation

AMBER v10 [16] software package was used to determine the molecular dynamics (MD) structures of the neamine species by Particle Mesh Ewald method [16] in explicit solvent environment and to implement Nudged Elastic Band (NEB) [16–18] transition state analysis in implicit water environment. AM1-BCC [19] partial atomic charges of molecules were determined by the antechamber [20] module of AMBER v10. Parm99SB [21] parameters were used to neutralize neamine structures with Cl^- ions followed by solvation in TIP3 water box. After 1000 iterations of a short minimization and 10 ps of temperature equilibration steps, the solvated neamine structures were exposed to 10 ns of molecular dynamics. The primary neamine species, tetra-/tri-/di-protonated states (nea-4H/3H/2H), were not restrained during explicit solvent simulations. Ring II of the secondary neamine species, di-protonated state only (nea-2h), was restrained to a $^6rH_1$ relaxed half-chair conformer during explicit solvent simulations. R.m.s.d. analysis, transglycosidic distance measurements, H-bonding and cluster analysis through the trajectories of the explicit solvent simulations were implemented by the *ptraj* module of AMBER v10.

NEB transition state analysis was performed on a model compound, 4-methoxy-2-deoxystreptamine (MODOS), shown in Fig. 2. A NEB transition state pathway energy plot was constructed out of 30 frames between two end-point ring conformers, $^4C_1$ and $^6S_2$, of MODOS.

Three staggered gg, gt and tg exocyclic rotamer populations for the low-energy structures of the primary and secondary neamine species were determined by the Boltzmann distribution law [22,23]. According to the Bolztmann's distribution law, a fractional probability of a rotamer population $P_{(\omega)}$ at a given temperature is

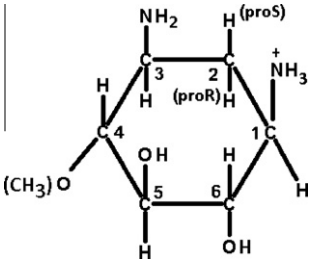

Fig. 2. Haworth formula of 4-methoxy-2-deoxystreptamine (MODOS). MODOS was used as a model compound to study ring II of neamine by Nudged Elastic Band (NEB) [16–18] transition state analysis.

expressed by Eq. (8), where ω refers to one of the three staggered rotamers (gg, gt or tg), $P_{gg} + P_{gt} + P_{tg} = 1$, $\Delta U(R)$ is the difference in cal/mol between two energy minima, one of which must be the lowest one. R is the ideal gas constant (1987 cal/K mol) and T is the temperature in K (298.15 K). $\Delta U(R)$ for the lowest energy minimum itself then becomes zero.

$$P_\omega = [\exp^{(-\Delta U(R)_\omega/RT)}]/[\exp^{(-\Delta U(R)gg/RT)} + \exp^{(-\Delta U(R)gt/RT)} + \exp^{(-\Delta U(R)tg/RT)}] \quad (8)$$

3. Results and discussion

3.1. pKa values

Potentiometric titration experiments revealed that the amino groups of neamine are all protonated (tetra-protonated state, nea-4H) below pH 4.5 and deprotonated above pH 9 (Fig. 3).

p*K*a values for the amino groups of neamine were determined by NMR titration experiments as described in Section 2.2. Chemical shifts for the primary proton peaks vicinal to the amino groups (e.g., H1 of $N1H_3^+$) were plotted versus pD (from 3.3 to 8.7). Fig. 4A–D illustrate the best-fit p*K*a curves fitted by Origin Software v.6 using Eq. (1) as a function of δ_{obs} in ppm (on the *y*-axis) and pD (on the *x*-axis). The NMR chemical shifts (δ_{obs}) for the H3, H2′, H1 and $H6'^{UF}$ (UF: upfield) proton peaks were used to determine the p*K*a1 of N3 (p*K*a1-N3, 6.44 ± 0.13, R^2 = 0.96), Fig. 4A, p*K*a2 of N2′ (p*K*a2-N2′, 7.23 ± 0.09, R^2 = 0.97), Fig. 4B, p*K*a3 of N1 (p*K*a3-N1, 7.77 ± 0.19, R^2 = 0.94), Fig. 4C, and p*K*a4 of N6′ (p*K*a4-N6′, 8.08 ± 0.15, R^2 = 0.93), Fig. 4D, respectively.

Table 1 compares the p*K*a values reported in this paper by ^1H NMR titration studies in D_2O (Table 1d and Fig. 4A–D) to the literature p*K*a values of neamine-related moieties of neomycin B by ^{15}N NMR by Botto and Coxon [24] (Table 1a), gentamycin C1 by ^1H

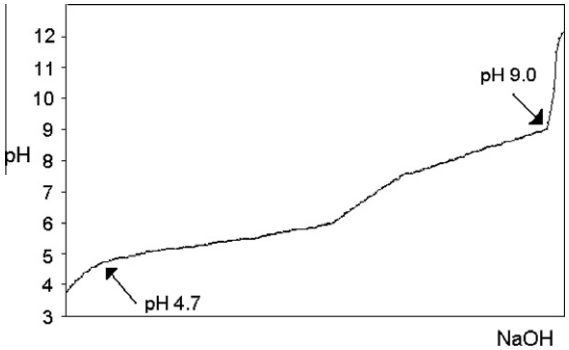

Fig. 3. Potentiometric base-titration between pH ~3.7 and ~12.0 for neamine. Neamine looses its buffering capacity below pH 4.7 and above pH 9.0. 10 μL increments of 0.5 N NaOH was used to titrate the neamine solution.

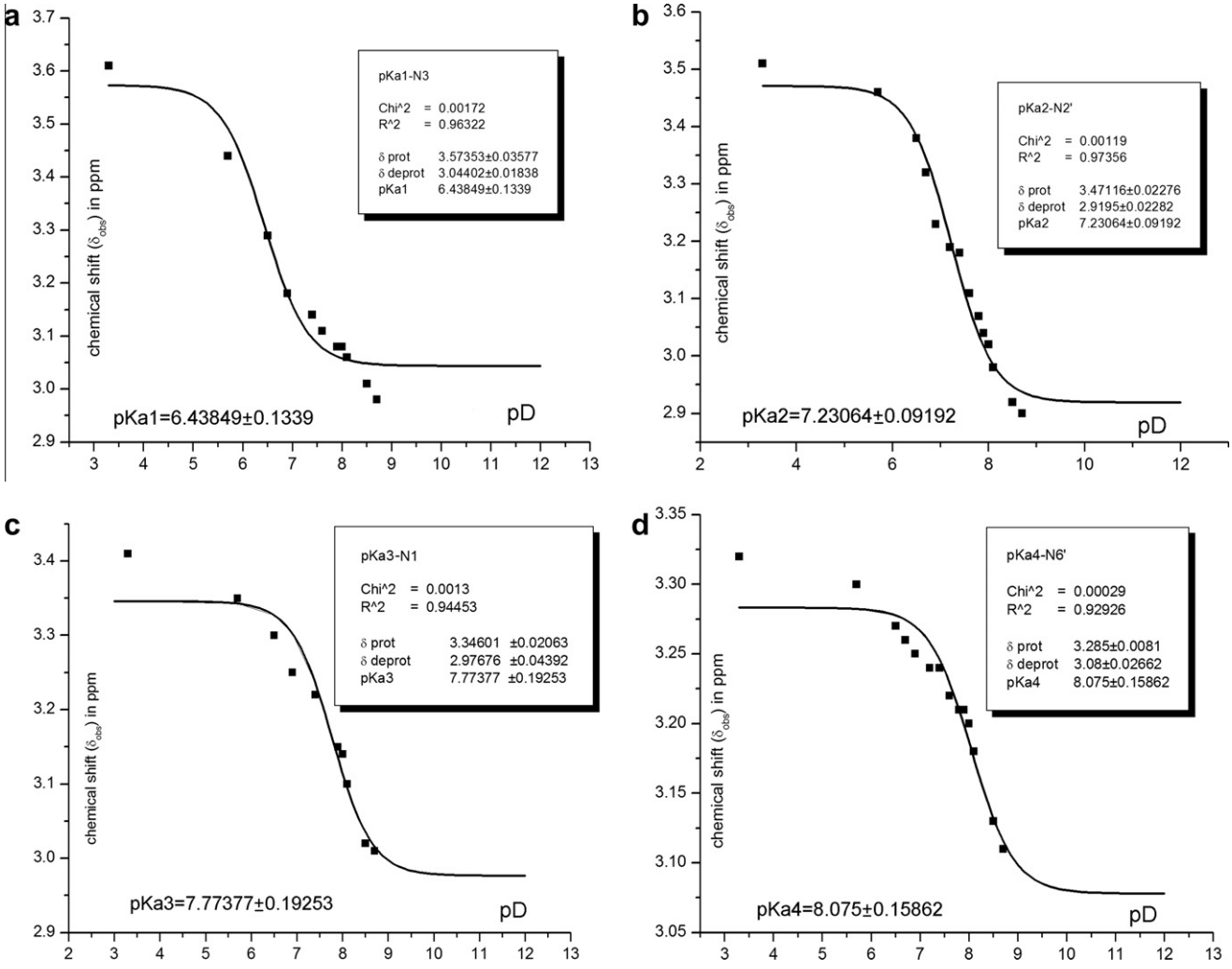

Fig. 4. The p*K*a curves were determined using Eq. (1) for (A) p*K*a1 of the N3 amino group, (B) p*K*a2 of the N2′ amino group, (C) p*K*a3 of the N1 amino group and (D) p*K*a4 of the N6′ amino group. The squared regression (R^2), upper (δ_{prot}) and lower (δ_{deprot}) chemical shift boundaries and the p*K*a values are printed next to the curves within the boxes. The p*K*a values are also presented in larger type letters to the left of the curves.

Table 1
p*K*a values of neamine and neamine-related moieties of aminoglycoside antibiotics.

	p*K*a1-N3	p*K*a2-N2′	p*K*a3-N1	p*K*a4-N6′
Neamine moiety of neomycin B[a]	5.74 ± 0.04	7.55 ± 0.04	8.04 ± 0.03	8.60 ± 0.02
Neamine moiety of gentamycin C1[b]	6.19 ± 0.40	7.40 ± 0.20	7.67 ± 0.40	9.86 ± 0.40
Neamine – Sutrisno et al.[c]	6.35 ± 0.20	n.r.	7.73 ± 0.15	8.62 ± 0.08
Neamine – Andac et al.[d]	6.44 ± 0.13	7.23 ± 0.09	7.77 ± 0.19	8.08 ± 0.15

n.r.: not reported.
[a] By ^{15}N NMR in H_2O/D_2O (85/15) by Botto et al. [24].
[b] By ^{1}H NMR in D_2O by Schacht et al. [25].
[c] By potentiometric titration in H_2O by Sutrisno et al. [26], where p*K*a values were assigned by comparison to a and b.
[d] Fig. 4A–D by ^{1}H NMR in D_2O (work in this thesis).

NMR by Schacht et al. [25] (Table 1b), and neamine by potentiometric titration in H_2O by Sutrisno et al. [26] (Table 1c). Indeed, Sutrisno et al. published three unassigned p*K*a values of 6.35 ± 0.20, 7.73 ± 0.15 and 8.62 ± 0.08 out of four expected p*K*a values. The p*K*a assignment given in Table 5c for Sutrisno et al. data was estimated in this paper by comparing to the p*K*a values of Botto et al. (Table 1a) and of Schacht et al. (Table 1b).

Considering the percent error ranges given in Table 1 for the p*K*a values of the neamine work in this thesis and of the work of the other authors, the difference between the corresponding p*K*a values may range up to 1.23 pH/D units, which may possibly arise from the different techniques applied to measure the p*K*a points. Also, the presence of a substituent on neamine, as in neomycin B or gentamycin C1, may bring about intra-molecular interactions such as an inter-residual bifurcated H-bond from an N2′ hydrogen of ring I to O4″ and O5″ of ring III in neomycin B [27], which should be considered potential factors for p*K*a shifts. It should also be noted that there is usually some difference between p*K*a values measured in H_2O and D_2O [28], whose relationship is arbitrary and it very much depends on the compound studied, the ionic

strength of the solvent(s), and the techniques used. At present a correct/adequate extrapolation of p*K*a(D_2O) values to aqueous phase p*K*a(H_2O) values is not possible when different titration techniques are involved, as in the present case.

3.2. Presence of primary, secondary and tertiary neamine species and proton chemical shifts

Basically three neamine samples at pD 3.3, 6.5 and 7.4 were studied in details by 1D/2D NMR techniques. Neamine at pD 3.3 (nea33) was chosen to ascertain that in one set of experiments all amino groups are fully in their protonated states (nea-4H). Neamine at pD 6.5 (nea65) was chosen because it gains three proton charges at this pD and it is assumed that the N2′, N6′ and N1 amino groups are then completely protonated (nea-3H). Neamine at pD 7.4 (nea74) was selected to determine the unbound conformation of neamine under physiological conditions. Presumably neamine gaines 2 (nea-2H, where N6′ and N1 amino groups are completely protonated) or 3 (nea-3H, similar to nea65) proton charges at pD 7.4.

At least two distinct neamine species were discovered in different concentrations, which exhibit slow exchange rates around physiological pH, pD ~7.4, and at pD 6.5 in low-salt media. They are denoted as nea74p and nea65p, respectively, for the primary/major and nea74s and nea65s, respectively, for the secondary/minor conformers. Fig. 5 shows an overlay plot of ^{1}H NMR spectra of neamine between pD 3.3 and 8.7. The h1′ peaks of the secondary neamine species are marked with arrows and lowercase. The H1′ peaks of the primary neamine species, marked with H1′ in Fig. 5, resonate downfield from the h1′ peaks. In this region these peaks rise steadily between pH 6.9 and 8.0, giving the highest concentration of ~18.4% in molar concentration (averaged out of several determinations) at pD 7.4 at 25 °C, but rapidly fade outside this maximal region.

Fig. 6 concentrates on the spectral regions of the H(h)2^{proR} (on the left) and H(h)2^{proS} (on the right) proton peaks of a nea74 sample, Fig. 6A, showing the primary and secondary neamine species, and another spectrum of the same neamine sample kept at room temperature for 3 years, Fig. 6B, which yielded a trace amount of a tertiary/micro neamine species (~3%), named nea74t for this reason, associated with the smallest proton peaks marked with italic lowercase letters at the bottom spectrum. To the best of our knowledge, this is the first time that the presence of a secondary and tertiary neamine species in low-salt media is being reported in literature.

Proton chemical shifts (δ, ppm) for rings I and II of nea33, nea65p, nea65s, nea74p, and nea74s are summarized in Table 2, which were determined by COSY, NOESY and HMBC type NMR experiments. Spectral assignments for H6′$^{(proR,proS)}$ prochiral protons were found to be equivocal. Therefore, the upfield H(h)6′ peak is denoted H(h)6′ ^{UF} and the downfield H(h)6′ peak is denoted H(h)6′^{DF}. The stereospecific assignment of the H/h2^{proR} and H/h2^{proS} peaks revealed that H(h)2^{proR} (~2.4 ppm) resonates downfield from H(h)2^{proS} (~1.8 ppm).

The H4 peaks of the primary neamine species at pD 3.3 and 6.5 were confirmed by gHMBC via a transglycosidic through-bond connection from H1′ of ring I to C4 of ring II (Appendix A). The unambiguous h4 peak assignment of the secondary neamine species at pD 6.5 and 7.4 as well as the primary H4 peak of neamine at pD 7.4 was confirmed by NOESY based on the strongest transglycosidic

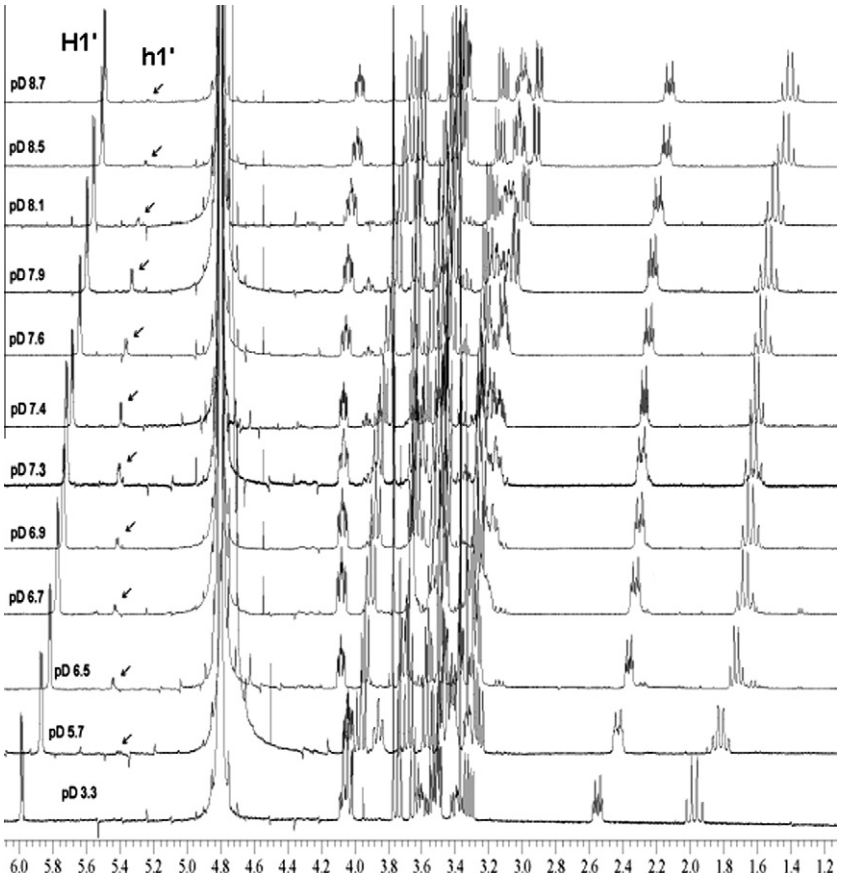

Fig. 5. Some selected overlayed NMR spectra between pD 3.3 and 8.7 showing chemical shifts of the 1′ proton-peaks (marked with arrows) for ring I of the secondary neamine species (and lower letter case). H1′ chemical shifts of the primary neamine species are also shown around 5.8 ppm in the figure.

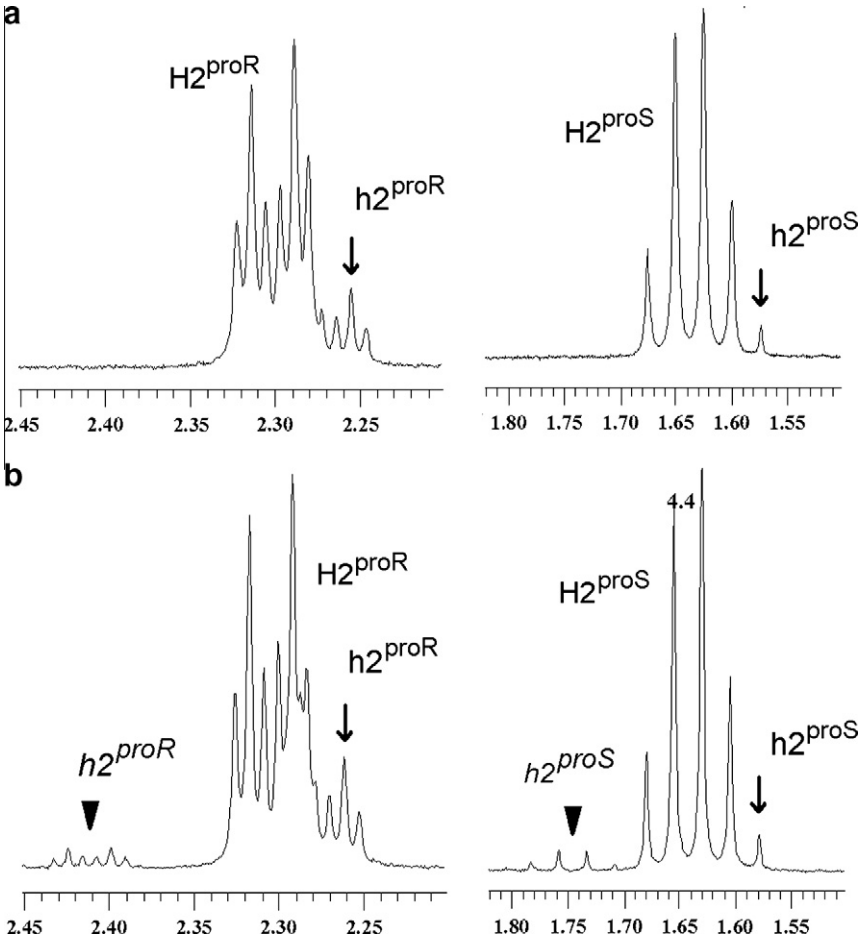

Fig. 6. Spectral regions of the H(h)2^{proR} (δ = 2.30 ppm) and H(h)2^{proS} (δ = 1.62 ppm) proton peaks of (A) a nea74 sample, showing the primary (~83%) and secondary (~17%) neamine species, and (B) the same nea74 sample kept at room temperature for 3 years, indicating the presence of a trace amount of a tertiary/micro neamine species (3.4% in concentration), where the percent molar concentrations for the primary and secondary species are ~73% and ~25%, respectively. ↓: peaks belonging to the secondary species nea74s and ▼: visible small peaks belonging to the tertiary species nea74t. The tertiary peaks are marked with italic lowercase letters while the secondary peaks are shown with lowercase letters.

Table 2
Proton chemical shifts determined for different neamine species chemical shifts [δ (ppm)].

	nea33	nea65p	nea65s	nea74p	nea74s
Ring I					
1′	5.99	5.82	5.44	5.68	5.39
2′	3.51	3.37	3.40	3.18	3.29
3′	4.05	3.94	3.91	3.83	3.86
4′	3.54	3.48	3.37	3.44	3.36
5′	4.08	4.08	3.93	4.08	3.93
6′(UF)	3.32	3.27	3.14	3.24	3.12
6′(DF)	3.53	3.49	3.48	3.46	3.47
Ring II					
1	3.41	3.29	3.68	3.20	3.67
2(proS)	1.99	1.72	1.63	1.60	1.61
2(proR)	2.57	2.37	2.28	2.28	2.27
3	3.61	3.28	3.28	3.14	3.12
4	4.06[a]	3.73[a]	3.51[b]	3.57[a]	3.47[b]
5	3.76	3.68	3.62	3.65	3.62
6	3.65	3.56	3.52	3.50	3.48

UF: upfield. DF: downfield.
[a] Confirmed by HMBC.
[b] Confirmed by NOESY. All other assignments were determined by COSY-type experiments.

NOE cross-peaks from h1′ to h4 and from H1′ to H4 (Appendix B), respectively, which greatly facilitated the COSY assignment of the rest of the ring II proton peaks.

Proton chemical shifts given in Table 2 together with the stack plots shown in Fig. 5 reveal that while a multitude of peaks of the primary neamine species exhibit drastic upfield chemical shifts as pD is increased, the chemical shifts of the secondary neamine species are rather pD tolerant between pD 6.5 and 8.5. For instance; the chemical shift difference for the H4 proton peaks of nea65p and nea74p is 0.25 ppm while this difference is only 0.04 ppm for the h4 proton peaks of nea65s and nea74s. As the pD is increased from 3.3 to 7.4, the greatest upfield shifts occur with H1′, H2′, H3′, H1, H2^{proS}, H2^{proR}, H3 and H4 of the primary neamine species.

It is clear that the greatest shifts between pD 3.3 and pD 7.4 involve protons in the vicinity of the titratible groups with the lowest p*K*a values such as p*K*a1-N3 (6.44 ± 0.13) for the H4/H3/H2$^{proR/S}$ shifts and p*K*a2-N2′ (7.23 ± 0.09) for the H3′/H2′/H1′ shifts. As shown in Fig. 3 a neamine amino group, presumably N3 of ring II (Fig. 1), begins to shed protons above pD 4.7 and it is suggested that an equilibrium constituted by two or more different protonated primary states of neamine that are in fast exchange on the NMR time scale begins to become established. A fast exchange would cause the NMR spectrum to reveal only one main compound with varying/shifting chemical shifts causing an apparent movement of single peaks. Because the p*K*a values for the N1 (p*K*a3-N1 = 7.77 ± 0.19) and N6′ (p*K*a4-N6′ = 8.08 ± 0.15) amino groups are greater than pD 7.4, these amino groups of the primary

neamine species are mainly in their protonated forms at pD 7.4 and thus the nearby proton chemical shifts are less affected by pH changes between pD 3.3 and pD 7.4.

With p*K*a2-N2′ being 7.23 ± 0.09, Fig. 4B, it seems likely that the secondary neamine species reaches a maximum concentration at pD 7.4, where the di-protonated state of the secondary neamine species (nea-2h) is more populated than its tri-protonated counterpart (nea-3h). Thus, it is possible that only the nea-2h, where the N6′ and N1 amino groups are protonated, exists near the transition state (described in Section 3.4). Presumably, nea-3h is not electrostatically stable and is immediately converted to the tri-protonated state of the primary neamine species (nea-3H) at fast exchange rates, leaving nea-2h as the only secondary neamine species that is in slow exchange with the primary neamine species in aqueous medium at pD ~7,4. As pD is decreased, the concentration of nea-3H increases, which gradually decreases the population of nea-2h down to zero at pD 5.7. When pD is increased, the concentration of mono-protonated primary neamine species (nea-H), where only the N6′ amino group is protonated, increases lowering the concentration of nea-2h. This proposed transition state theory seems to be the most likely explanation why the secondary proton peaks are sheltered from drastic shifts upon pH changes.

Despite the fact that only a few tertiary proton assignments were made for nea74t and that nea74t was not studied at other pHs, it seems likely that the micro species exist in a di-protonated state and that the chemical shifts are pD independent, just as discussed above for the secondary species nea-2 h.

3.3. Exchange rate constants

As briefly mentioned in Section 3.2 and shown in Fig. 6A, neamine at pD 7.4 (nea74) initially revealed two slowly exchanging main species in low-salt media, which are termed primary (nea74p) for the high concentration (~%82) species and secondary (nea74s) for the low concentration (~%18) species. Exchange rates, k_{PS} and k_{SP} in Eq. (2), between nea74p (P state) and nea74s (S state) were determined using the spin–spin (transverse) relaxation times (T 2) of nea74p and nea74s, $T\,2_P$ by Eq. (6) and $T\,2_S$ by Eq. (7), respectively, in which $\Delta\nu_{1/2(P)}$ and $\Delta\nu_{1/2(S)}$ were measured off the line-width at the half height of the H1′ and h1′ proton peaks, respectively, on the ^{1}H NMR spectrum of nea74 as shown in Fig. 7. $\Delta\nu_{1/2(P)}$ and $\Delta\nu_{1/2(S)}$ were measured as 2.54 Hz and 2.95 Hz, respectively, in the absolute intensity mode so that the peak heights could be compared to each other by the deconvolution (line-fitting) function of the Varian v6.1C software.

Determination of the exchange rate constants, k_{PS} in Eq. (3) and k_{SP} in Eq. (4), also depends on T 2 at fast exchange rates, which is determined by Eq. (5). $\Delta\nu_{1/2}$ in Eq. (5) requires a high temperature NMR experiment to allow the H1′ and h1′ peaks to merge into a single peak at fast exchange. However, such an experiment with neamine was not carried out. Instead, $\Delta\nu_{1/2}$ was taken from the measured H1′ peak width of 1.71 Hz of nea33 at 25 °C, assuming that a single H1′ peak at acidic pH at 25 °C would be virtually identical to a merged H1′ peak at pD 7.4 at a higher temperature.

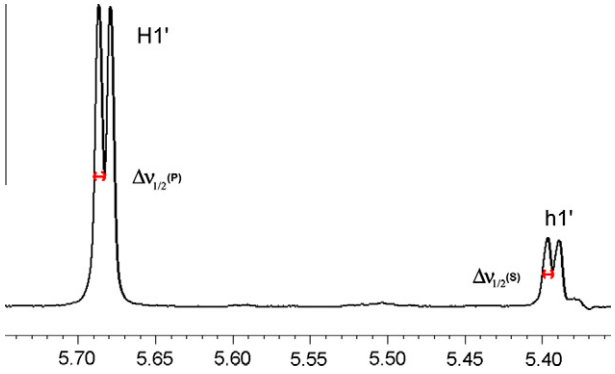

Fig. 7. Anomeric proton peaks H1′ and h1′ for the P and S states of neamine at pD 7.4. ↔ in the figure marks the line-widths at the half height ($\Delta\nu_{1/2}$) of the H1′ and h1′ proton peaks assigned for the P and S states of neamine at pD 7.4 and 25 °C, respectively.

Based on the approximated $\Delta\nu_{1/2(P)}$, $\Delta\nu_{1/2(S)}$ and $\Delta\nu_{1/2}$ values given above, the derived k_{PS}, k_{SP} and K_{ex} (=k_{PS}/k_{SP}) rate constants are listed in Table 3. The frequency (Hz) of the k_{PS} and k_{SP} exchange rates are inversely proportional to the life-time of the P ($\tau_P = 1/k_{SP}$) and S ($\tau_S = 1/k_{PS}$) states, respectively. This means that nea74p exists at a lower frequency of 2.63 Hz (k_{PS}) with a longer τ_P of 0.38 s on the NMR time scale as compared to nea74s which appears at a relatively higher frequency of 3.85 Hz (k_{SP}) due to a shorter τ_S of 0.25 s. The exchange rate constant at equilibrium (K_{ex}) is less than 1 (0.77) suggesting that the direction of the exchange favors nea74p in aqueous solution at 25 °C. This appears to be the first time that these kinetics parameters have been reported for neamine existing in two conformational states at pD 7.4 at 25 °C.

Exchange rates between nea74t and other neamine species could not be determined due to a very low signal-to-noise ratio.

3.4. Neamine endocyclic dihedral angles and ring conformers

Vicinal proton-proton coupling constants, $^3J_{HH}$, listed in Table 4 were determined by deconvolution analysis on high resolution ^{1}H NMR spectra of neamine at pD 3.3, 6.5, and 7.4. The corresponding endocyclic dihedral angles were determined by applying the $^3J_{HH}$ values in an empirically generalized Karplus-like equation developed by Haasnoot–Leuuw–Altona (HLA) [15] which includes β-substituent corrections optimized for three and four substituents in conformationally rigid six-membered ring systems. The resulting HLA torsion angles (HLA°) for nea33, nea65p, nea65s, nea74p, nea74s and nea74t were reported in Table 2 as t (trans) for torsion angles around 180°, g^+ (gauche$^+$) for those around + 60°, g^- (gauche$^-$) for those around −60°. The h3–h4 torsion angle for nea74s is not reported in Table 4 as $^3J_{h3-h4}$ could not be determined due to severe spectral overlaps on the h3 and h4 peaks. Also the *h3–h4*, *h4–h5*, *h5–h6*, *h6–h1* torsion angles of nea74t are not reported because the *h1*, *h3*, *h4*, *h5* and *h6* peaks could not be assigned due to low signal-to-noise ratio.

The most likely theoretical ring conformers of neamine are $^4C_1$, $_4C^1$, $^2S_0$ for ring I, presented in Table 5 $^4C_1$, $_4C^1$, $^6S_2$, $^6rH_1$ (“relaxed half-chair”) for ring II, presented in Table 6, whose HLA° torsion angles were determined upon fusing neamine rings I and II substituents with the carbon frame of the $^4C_1$ conformations for ring I and ring II of the kanamycin X-ray structure, Cambridge Structural Database CSD ID: 610593 [29], the $_4C^1$ conformation for ring IV of neomycin B in complex with 16S rRNA, X-ray structure PDB ID: 2ET 4 [30], and the $^2S_0$ (of ring I) and $^6S_2$ (of ring II) conformations for the iduronate residue of an heparin derivative in complex with a basic fibroblast growth factor, NMR structure PDB ID: 1BFC [31]. The rH conformer is thought to be an intermediate state between the S and H conformers. The generic HLA° torsion angles for the $^6rH_1$ conformation of ring II of the secondary neamine structure were determined by NEB transition state analysis between $^4C_1$

Table 3
Rate constants and life-times characterizing neamine conformational exchange at pD 7.4.

k_{PS}(=1/τ_S)	nea74p → nea74s	2.63 s^{-1} (Hz)
k_{SP}(=1/τ_P)	nea74s → nea74p	3.85 s^{-1} (Hz)
Kex(=k_{PS}/k_{SP})	nea74p ↔ nea74s	0.77

Table 4
Experimental $^3J_{HH}$ (Hz) values and theoretical HLA (Haasnoot, De Leeuw and Altona) [15] dihedral angles (HLA°) of different neamine species.

	nea33 $^3J_{HH}$/HLA°	nea65p $^3J_{HH}$/HLA°	nea65s $^3J_{HH}$/HLA°	nea74p $^3J_{HH}$/HLA°	nea74s $^3J_{HH}$/HLA°	nea74t $^3J_{HH}$/HLA°
Ring I						
1′–2′	3.890/g^+	3.802/g^+	3.769/g^+	3.832/g^+	3.667/g^+	3.63/g^+
2′–3′	10.957/t	10.812/t	10.305/t	10.628/t	10.526/t	7.97/t
3′–4′	9.272/t	9.118/t	9.191/t	9.308/t	9.343/t	9.5/t
4′–5′	9.851/t	9.828/t	9.410/t	9.764/t	9.745/t	9.5/t
Ring II						
1–2(R)	4.299/g^-	4.277/g^-	4.606/g^-	4.152/g^-	4.493/g^-	4.18/g^-
1–2(S)	12.514/t	12.504/t	12.677/t	12.539/t	12.598/t	12.37/t
2(R)-3	4.215/g^+	4.195/g^+	4.151/g^+	4.314/g^+	4.151/g^+	4.18/g^+
2(S)-3	12.617/t	12.402/t	12.677/t	12.409/t	12.635/t	12.37/t
3–4	10.185/t	9.618/t	3.240/∼−120°	9.519/t	nd/nd	nd/nd
4–5	9.265/t	9.263/t	9.334/t	9.278/t	9.175/t	nd/nd
5–6	9.283/t	9.005/t	9.360/t	9.305/t	9.211/t	nd/nd
6–1	10.374/t	10.253/t	10.089/t	10.084/t	10.202/t	nd/nd

g^+: 60°; g^-: −60°; t: 180°; nd: not determined.

Table 5
Averaged $^3J_{HH}$ (Hz) and torsion angles (HLA°) for chair (C) and skew (S) conformers of ring I.

Torsion	$^4C_1$		$_4C^1$		^2S_o	
	$^3J_{HH}$	HLA°	$^3J_{HH}$	HLA°	$^3J_{HH}$	HLA°
1′–2′	∼2–4	g^+	∼ 2–4	g^-	∼ 2–4	∼30°
2′–3′	∼9–12	t	∼ 2–4	g^-	∼ 9–12	t
3′–4′	∼9–12	t	∼ 2–4	g^+	∼ 9–12	t
4′–5′	∼9–12	t	∼ 2–4	g^+	∼ 2–4	∼ −120°

HLA°: Torsion angle by HLA (Haasnoot, De Leeuw and Altona) [15]; g^+: ∼60°; g^-: ∼−60°; t: ∼180°.

and $^6S_2$ ring conformers of MODOS (Fig. 2), Section 2.5. An energy plot of the NEB transition state pathway for MODOS was constructed out of 30 frames as shown in Fig. 8, in which frame #16, an intermediate energy structure of MODOS with $^6rH_1$ conformation, was found to best fit the HLA° torsion angles given for nea65s in Table 4. Therefore, the structure coordinates of frame#16 were used to generalize HLA° dihedral angles in Table 6 for likely $^6rH_1$ conformation of ring II.

Comparison of the data presented in Tables 5 and 6 to those presented in Table 4 strongly suggests that rings I and II of the primary neamine species as well as ring I of the secondary species adopt the $^4C_1$ chair conformation, shown in Fig. 9A for ring I and Fig. 9B for ring II.

The NMR data for nea65s presented in Table 4 seem to be most consistent with HLA° values for a $^6rH_1$ conformer given in Table 6, whose structure is shown in Fig. 9C. However it should be noted that the theoretical $^3J_{HH}$ range given in Table 6 for the H4–H5 (1.5–4 Hz for a 130° dihedral angle) and H3–H4 (∼2–5 Hz for ∼−130° dihedral angle) vicinal proton systems of the $^6rH_1$ ring II conformer are not consistent with the experimental $^3J_{h4h5}$ (9.33 Hz) and $^3J_{h3h4}$ (3.24 Hz) values, respectively, given in Table 4 for nea65s. The assumption with the HLA equations is that the $^3J_{HH}$ values to be used is biased towards torsion angles ±60° and 180° on stable structures of rigid six-membered rings, for which coupling constants occur in the ranges 0–5.5 Hz and 7.5–13 Hz, respectively [15]. Considering that there is noticeable conformational as well as vibrational flexibility concerning the C3–C4–C5 bonds of ring II of the secondary neamine species, the HLA° value listed in Table 4 for the h4-h5 (t) and h3–h4 (∼−120°) vicinal protons of nea65s, are possibly not representing the genuine dihedral angles, which indeed should be about 130° and ∼−130°, respectively.

As seen in Table 4 $^3J_{h3-h4}$ of nea74s could not be determined due to spectral overlaps which incapacitated deconvolution analysis and coupling constant measurements for the h3 and h4 peaks of nea74s. Nevertheless, the ring II structure of the secondary neamine species is assumed to adopt a single conformation around the physiological pH as the chemical shifts of the secondary proton peaks are pH tolerant. Thus NMR and structural information gained for ring II of nea65s also applies to the ring II structure of nea74s.

Ring I of the tertiary neamine species, nea74t, possess torsion angles similar to those of nea65s and nea74s, Table 4, suggesting the presence of a $^4C_1$ chair conformer. It is known that the tertiary neamine species (nea74t) exists in the lowest concentration (∼3%) and it takes much longer time to form compared to the secondary neamine species. In addition, it is highly likely that the ring II structure for the tertiary neamine species does not differ much from that of the secondary species due to similar $^3J_{HH}$ values involving the h3/h2/h1 vicinal protons as reported in Table 4 for nea65s and nea74t. Yet, the tertiary neamine species should be energetically higher (less stable) than the $^6rH_1$ conformer of nea65s in

Table 6
Generalized $^3J_{HH}$ (Hz) and torsion angles, HLA°, for chair (C), skew (S) and hypothetical relaxed half-chair, rH, conformers of ring II of neamine.

Torsion	$^4C_1$		$_4C^1$		^2S_o		$^6rH_1$	
	$^3J_{HH}$	HLA°	$^3J_{HH}$	HLA°	$^3J_{HH}$	HLA°	$^3J_{HH}$	HLA°
$1–2^{proR}$	∼1.5–5	g^-	∼1.5–5	g^+	∼1.5–5	g^+	∼1.5–5	g^-
$1–2^{proS}$	∼11–13	t	∼1.5–5	g^-	∼1.5–5	g^-	∼11–13	t
$2^{proR}–3$	∼2–5	g^+	∼2–5	g^-	∼2–5	g^-	∼8–3.5	30° -g^+
$2^{proS}–3$	∼11–13	t	∼2–5	g^+	∼2–5	g^+	∼9–12	150°-t
3–4	∼9–11	t	∼1–4	g^-	∼0.9–1.7	∼−100°	∼2–5	∼−130°
4–5	∼7–10	t	∼3–5	g^+	∼7–10	t	∼1.5–4	130°
5–6	∼7–10	t	∼3–5	g^-	∼7–10	t	∼7–10	t
6–1	∼9–11	t	∼3–5	g^+	∼4.9–7.9	∼150°	∼9–11	t

HLA°: Torsion angle by HLA (Haasnoot et al.) [15]; g^+: ∼60°; g^-: ∼ −60°; t: ∼180°.

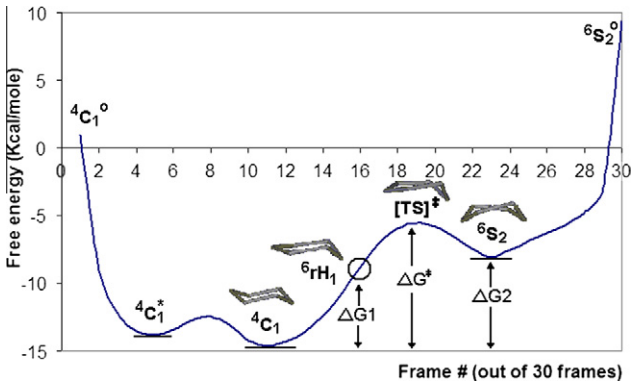

Fig. 8. Nudged Elastic Band (NEB) transition state pathway energy plot of 4-methoxy-2-deoxystreptamine (MODOS). Position of the high-energy starting coordinates of $^4C_1{}^o$ chair [frame 1; 0.9213 kcal/mol], low-energy $^4C_1{}^*$ chair [frame 5; −13.8339 kcal/mol], lowest energy $^4C_1$ chair [frame 11; −14.6616 kcal/mol], $^6rH_1$ relaxed half-chair frame 16 (circled); −8.8066 kcal/mol], TS‡ transition state [frame 19; −5.5199 kcal/mol], $^6S_2$ skew [frame 23; −8.0708 kcal/mol], and high energy end-point coordinates of $^6S_2{}^o$ skew [frame 30; 9.4554 kcal/mol] conformers are marked on the plot. Δ*G*1 is the energy difference (5.855 kcal/mol) between $^4C_1$ and $^6rH_1$, ΔG‡ is the energy difference (9.1417 kcal/mol) between $^4C_1$ and TS‡ and Δ*G*2 is the energy difference (6.5908 kcal/mol) between $^4C_1$ and $^6S_2$. For simplicity only carbon structures are shown for $^4C_1$, $^6rH_1$, TS‡ and $^6S_2$.

the NEB transition state (TS) pathway, frame 16 in Fig. 8, but much less than the hypothetical TS for the $^2H_1$ half-chair conformer, frame 19 in Fig. 8, as the population at TS is zero. Giving that the energy barrier between the $^4C_1$ (frame 11 in Fig. 8) and $^2S_0$ (frame 23 in Fig. 8) minima is too high to allow the $^4C_1 \rightarrow {}^2S_0$ conversion, $\Delta G^{\ddagger} = 9.1417$ kcal/mol, nea74t is more likely to be somewhere at frame 17 (−7.1016 kcal/mol) in Fig. 8, a less stable structure that approaches a half-chair conformation at the transition state.

It should be noted that the $^6rH_1$ conformer of the secondary (nea65s/74s) as well as the tertiary (nea74t) neamine species do not sit in a minimum in Fig. 8. To clearly image this, a hypothetical TS energy plot was sketched in Fig. 10 to show the expected energy minima and the energy barriers, $A^{\ddagger}$ and $B^{\ddagger}$, for the proposed $^6rH_1$ ring II conformers of nea65s/74s and nea74t, respectively. These energy barriers are not seen in Fig. 8 because the application of existing algorithms of quantum chemistry and molecular dynamics to study reaction mechanisms involving changes in pyranose and cyclohexane conformations are not straightforward in times when there is a multitude of possible conformations/constraints along the pathway [32].

3.5. Through-space transglycosidic NOEs

Due to spectral overlaps, intensities for many of the intra-residual NOESY cross-peaks of the neamine species could not be resolved and inter-residual NOESY cross-peaks not involving H(h)1′ of ring I were likewise essentially inaccessible. Nevertheless, a majority of the transglycosidic NOESY cross-peaks from the anomeric proton H1′ of ring I to H3, H4, and H5 of ring II were unambiguously located by their proton chemical shifts and they were taken into account in the determination of transglycosidic neamine geometries.

Transglycosidic H(h)1′–H(h)3/4/5 NOESY cross-peak intensities measured in phase-sensitive mode [33] are given in Table 7. It should be noted that the h4 and h6 peaks of the secondary neamine species, nea65s and nea74s, severely overlap, see Table 2. Thus the h1′–h4 NOE intensities given in Table 7 include a negligible amount of h1′–h6 NOE volume. Also, the transglycosidic the (H/h)1′–(H/h)3 NOESY cross-peaks were found to be very weak (>5 Å) which disabled NOE measurements in some cases.

In all cases studied the transglycosidic NOE intensities, (H/h)1′–(H/h)3, (H/h)1′–(H/h)4 and (H/h)1′–(H/h)5, were found to be positive, indicating some degree of flexibility about the glycosidic bonds [34].

In NMR studies of neamine/paromamine-like aminoglycosides, cross relaxation rates or magnitudes of transglycosidic NOE intensities of $\mathbf{I}_{H1'-H3}$, $\mathbf{I}_{H1'-H4}$ and $\mathbf{I}_{H1'-H5}$ for H1′–H3, H1′–H4 and H1′–H5 through-space connectivities, respectively, between ring I and II are major determinants of the syn-Ψ and anti-Ψ geometries

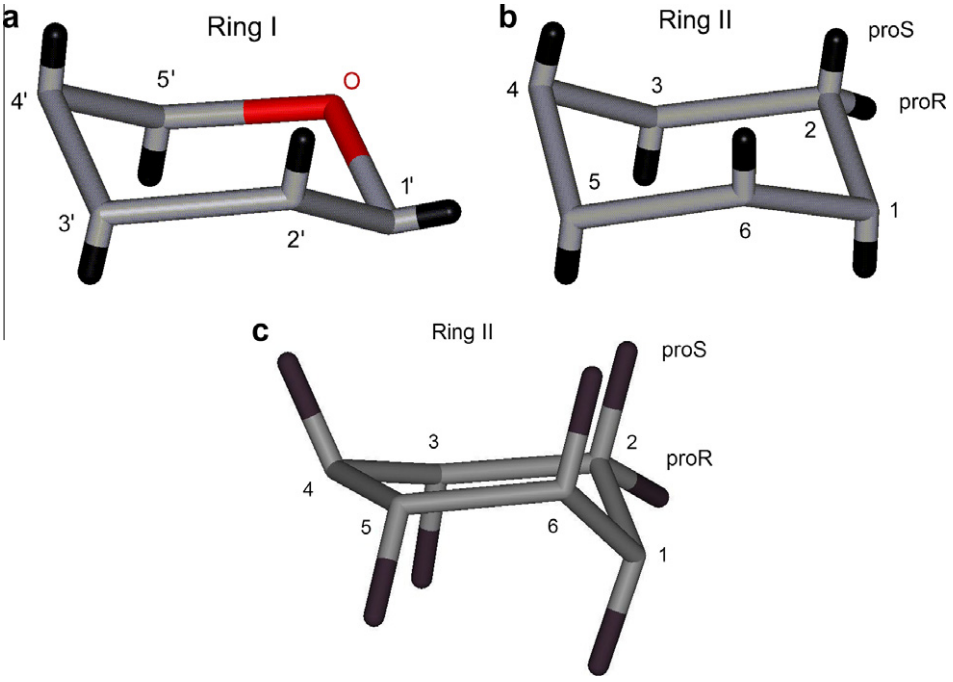

Fig. 9. Structures of neamine rings I and II. (A) $^4C_1$ chair conformation for ring I of nea33, nea65p, nea65s, nea74p and nea74s. (B) Ring II of nea33, nea65p and nea74p. (C) $^6rH_1$ relaxed half-chair conformation for ring II of nea65s and nea74s. Only protons attached to carbons are shown for simplicity.

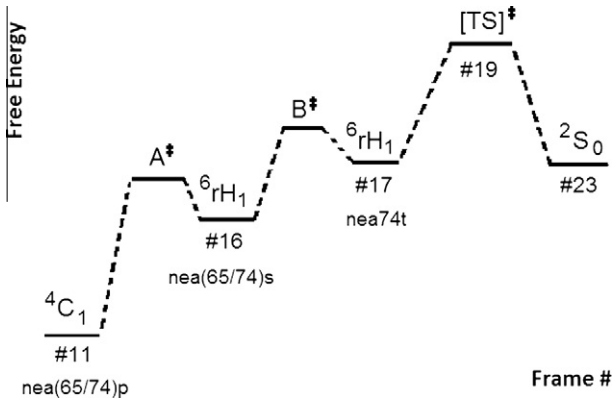

Fig. 10. Hypothetical transition state pathway energy plot of MODOS. This plot is presented to remedy the NEB transition state pathway energy plot shown in Fig. 8 which does not exhibit intermediary energy barriers $A^{\ddagger}$ and $B^{\ddagger}$ for the formation of $^{6}rH_1$ of the secondary neamine species nea(65/74)s (#16 in the figure, the same as frame 16 in Fig. 8) and of the tertiary neamine species nea74t (#17 in the figure, the same as frame 17 in Fig. 8), respectively.

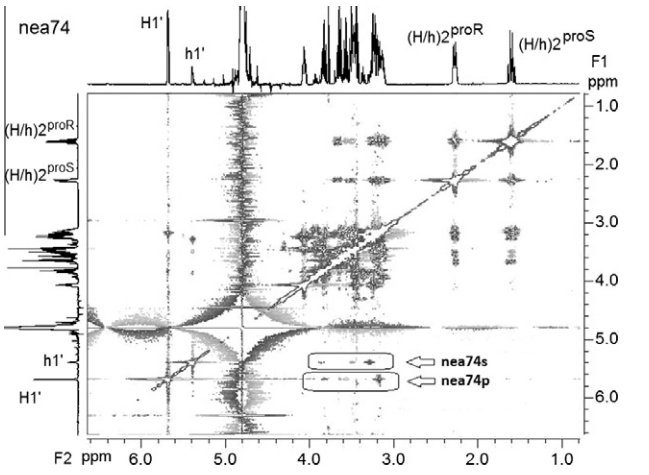

Fig. 11. NOESY spectrum of nea74. The primary and secondary transglycosidic NOESY cross-peaks from (H/h)1′ of ring I to (H/h)3/4/5 of ring II are boxed between 4.2 and 3 ppm along the F2 dimension. The NOESY FID was acquired with a mixing time of 75 ms.

Table 7
Transglycosidic NOE intensities given in integral units (iu). The NOESY cross-peaks were normalized by Mestre-C software to the corresponding inverted diagonal-peaks, H1′ for the primary species and h1′ for the secondary species, whose integral was set to −100,000 iu.

Protons	nea33	nea65p	nea65s	nea74p	nea74s
1′–3	105[a]	n.d.	n.d.	n.d.	n.d.
1′–4	1461[b]	581[c]	543[d]	544	687
1′–5	181	581[c]	n.d.	57	20

n.d.: not determined due to very low signal-to-noise ratio.
[a] Overlaps with H1′–H6 cross-peak.
[b] overlaps with H1′–H3′ and H1′–H5′ cross-peaks.
[c] H1′–H4 and H1′–H5′ cross-peaks overlap.
[d] overlaps with h1′–h6 cross-peak.

described in Section 1. In addition, NMR studies in literature revealed that aminoglycosides [27,34] as well as oligosaccharides [35] exhibit a mixture of syn-Ψ and anti-Ψ transglycosidic geometries in varying concentrations in free form in solution, the amount of which is governed by electrostatic configuration and pH [34]. Based on NMR data given in the literature these NOE intensities are rank ordered as $\mathbf{I}_{H1'-H4} \gg \mathbf{I}_{H1'-H5} > \mathbf{I}_{H1'-H3}$ for predominant syn-Ψ geometries (>95%) as in basic neomycin B [27] at pH 9.7 and acidic neamine [27] at pH 4.5. The rank ordering follows as $\mathbf{I}_{H1'-H5} \approx \mathbf{I}_{H1'-H3} \geqslant \mathbf{I}_{H1'-H4}$ for an equilibrium, for instance; between syn-Ψ (47%) and anti-Ψ (53%) geometries at fast exchange rates as in acidic kanamycin A [34] at pH 4.4.

Transglycosidic NOESY cross-peaks for the primary and secondary neamine species appear in two different transglycocidic NOE regions around physiological pH, including nea65p/s (data not shown) and nea74p/s, Fig. 11, in which the transglycosidic cross-peak regions are boxed and marked on F2 dimension accordingly. This can only occur if two molecular species interact at slow exchange rates and in this case presumably it occurs between the $^{4}C_1$ and $^{6}rH_1$ conformers of ring II, but is not due to a possible slow exchange between two distinct glycosidic geometries of neamine. Even if a slow exchange existed around the glycosidic bonds, it would be detected as split cross-peaks in a single transglycosidic NOESY region but not in two transglycosidic NOESY regions.

Transglycosidic NOESY cross-peak intensities $\mathbf{I}_{H1'-H3}$, $\mathbf{I}_{H1'-H4}$ and $\mathbf{I}_{H1'-H5}$ were measured in phase-sensitive mode and are listed in integral units (iu) in Table 8 for nea33, nea65p/s and nea74p/s. The transglycosidic H1′–H4 NOESY cross-peak of nea33 (1461 iu) was found to overlap with the intra-residual H1′–H3′ and H1′–H5′ NOESY cross-peaks at ~4.06 ppm, see Table 2. Given that ring I of the neamine species studied adopts a $^{4}C_1$ chair conformation, an average distance of ~3.8 Å may be attributed to the H1′–H3′ and H1′–H5′ distances of ring I based on molecular dynamics studies of neamine. Thus, the majority of the overlapping NOESY cross-peak around 4.06 ppm is due likely to $\mathbf{I}_{H1'-H4}$ of nea33. The transglycosidic H1′–H5 (δ = 3.65 ppm) and H1′–H3 (δ = 3.61 ppm) NOESY cross-peaks were observed to be mild (181 iu) and weak (105 iu), respectively, a finding which supports a syn-Ψ glycosidic geometry for nea33.

H1′–H4 and H1′–H5 NOESY cross-peaks of nea65p severely overlap around 3.70 ppm with a total integral volume of 581 iu. Nevertheless, a feeble $\mathbf{I}_{H1'-H3}$ observed at 3.28 ppm was indicative of a syn-Ψ geometry. Thus the NOESY cross-peak around 3.70 ppm is mainly attributed to the H1′–H4 NOE of nea65p. A strong h1′–h4 NOE (543 iu) of nea65s along with feeble h1′–h3 (δ = 3.28 ppm) and h1′–h5 (δ = 3.62 ppm) NOEs strongly suggested that nea65s adopt a syn-Ψ glycosidic geometry.

A strong H1′–H4 NOESY cross-peak (544 iu) at 3.57 ppm was observed for nea74p. In addition, a feeble H1′–H3 NOESY cross-peak at 3.14 ppm and a weak H1′–H5 cross-peak (57 iu) at 3.65 ppm strongly suggested a syn-Ψ geometry about the glycosidic bonds of nea74p. A strong NOESY cross-peak (687 iu) observed at 3.57 ppm was mainly attributed to the h1′–h4 NOE of nea74s. Similar to the NOE pattern observed with nea33/65s/65p/74p, the feeble h1′–h3 and weak h1′–h5 (20 iu) NOE intensities of nea74s are much less than that of the h1′–h4 peak, again strongly suggesting a syn-Ψ geometry.

In addition, it was found that the inter-residual (H/h)1′–(H/h)4 NOE intensities were slightly greater than the intra-residual (H/h)1′–(H/h)2′ NOE volumes, providing strong evidence for syn-Ψ geometry for all neamine species studied.

Table 8
Transglycosidic proton-proton distances (Å), ϕ (H1′–C1′–O–C4)/ψ (C1′–O–C4–H4) dihedral angles (°) and exocyclic rotamers ω (O5′–C5′–C6′–N6′)* for the best representative clustering coordinates out of 10 ns MD.

	H1′–H3	H1′–H4	H1′–H5	ϕ/ψ	ω
nea-4H	4.486	2.790	3.153	−41.5/−56.6	gg (%96)
nea-3H	4.510	2.541	3.434	−39.3/−26.7	gt (%99.3)
nea-2H	4.658	2.398	3.496	−26.7/−33.5	gt (%98.9)
nea-2h	4.364	2.555	2.982	−53.4/−14.7	gt (%99.5)

* Populations for the exocyclic rotamers were determined by the Boltzmann distribution law [22,23], Eq. (8).

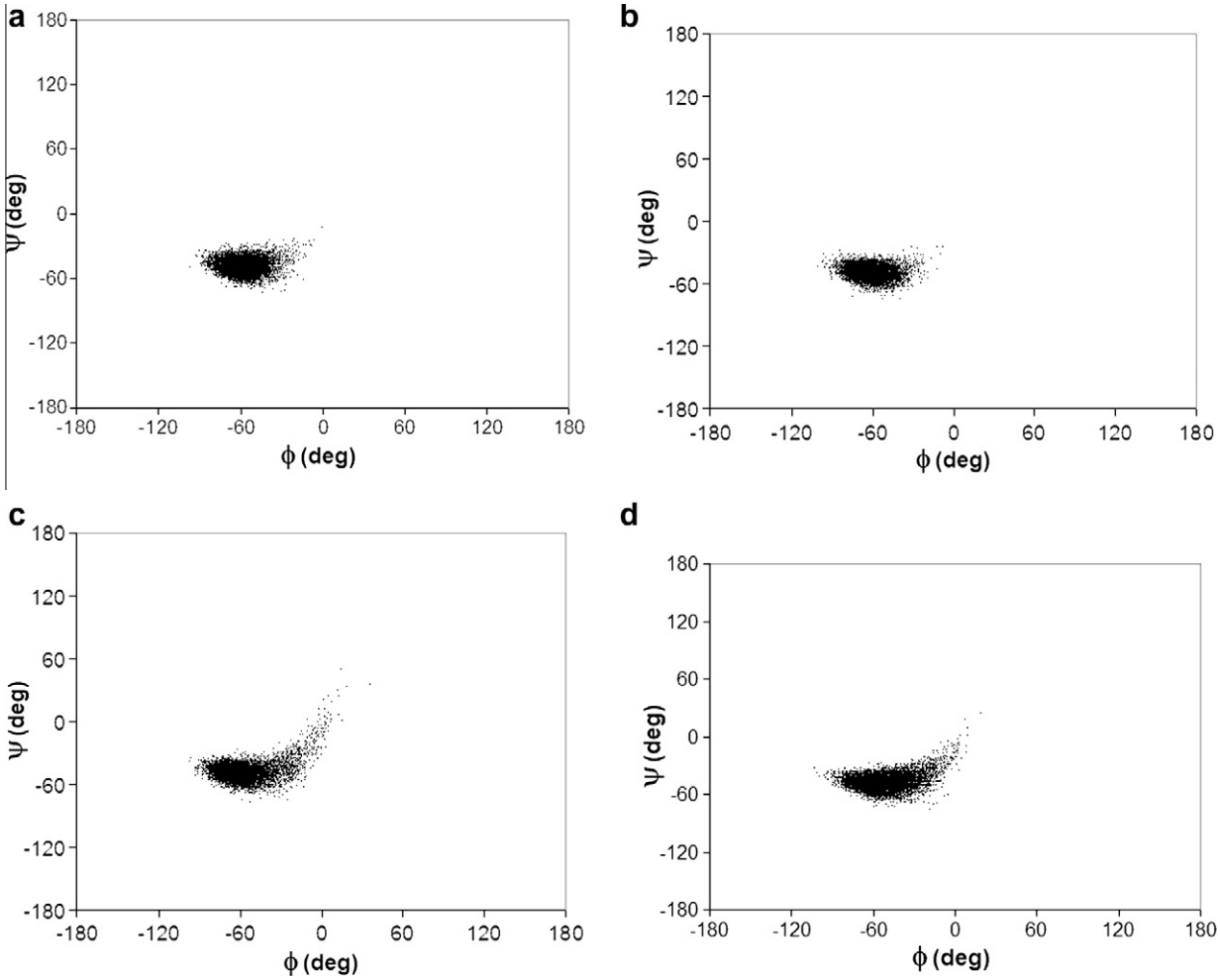

Fig. 12. Φ/Ψ plots of the neamine species corresponding to the last 5 ns of 10 ns MD. Φ (H1′–C1′–O–C4) on the *x*-axis was plotted versus Ψ (C1′–O–C4–H4) on the *y*-axis for (A) nea-4H (nea33), (B) nea-3H (nea65p and nea74p), (C) nea-2H (nea74p), and (D) nea-2h (nea65s, nea74s and possibly nea74t).

As a conclusion, magnitudes of the transglycosidic NOE intensities (**I**) presented in Table 8 for nea33, nea65p/s and nea74p/s were determined as $\mathbf{I}_{(H/h)1'-(H/h)4} \gg \mathbf{I}_{(H/h)1'-(H/h)5} > \mathbf{I}_{(H/h)1'-(H/h)3}$. This rank ordering is a strong indication of a negative syn-Ψ (where the Ψ dihedral angle is rotated counterclockwise) glycosidic geometry adopted in high concentrations by neamine at varying pD values, suggesting that the syn-Ψ geometry of neamine is very stable and independent of pH.

3.6. Molecular dynamics analysis

10 ns of explicit solvent MD computations were implemented for the primary neamine species, nea-4H/3H/2H, without using restraints and for the secondary neamine species, nea-2h, for which ring-II was restrained to the endocyclic carbon atom coordinates of MODOS with $^{6}rH_{1}$ relaxed half-chair conformer, obtained by NEB transition state analysis (frame #16 in Fig. 8). Ring I of the primary and secondary/tertiary neamine species and ring II of the primary neamine species adopted a stable $4C_1$ chair conformer during MD computations.

The Φ/Ψ plots shown in Fig. 12A for nea-4H (nea33), Fig. 12B for nea-3H (nea65p and nea74p), Fig. 12C for nea-2H (nea74p) and Fig. 12D for nea-2h (nea65s, nea74s and nea74t) strongly suggest negative syn-Ψ geometries, in which Φ/Ψ mostly populate around −60/−40, with the primary and secondary neamine species. Moreover nea-2H and nea-2h possess some flexibility about the glycosidic bonds which oscillate between negative syn-Ψ (Φ/Ψ = −50/−40) and positive syn-Ψ (Φ/Ψ = 10/0) geometries. These findings parallel the positive transglycosidic NOE connectivities observed with the neamine species mentioned in Section 3.5, indicating flexible rotations at fast exchange about the syn-Ψ geometry of the neamine species. Considering the magnitudes (**I**) of the transglycosidic NOEs, where $\mathbf{I}_{(H/h)1'-(H/h)4} \gg \mathbf{I}_{(H/h)1'-(H/h)5} > \mathbf{I}_{(H/h)1'-(H/h)3}$, the glycosidic fast exchange favors the negative syn-Ψ geometry in D_2O.

Transglycosidic proton-proton distances for the best representative cluster structures are given Table 8. As seen in the Table, the H(h)1′–H(h)4 distances are within the range of 1.8–2.8 Å for strong NOEs, those of H(h)1′–H(h)5 are within the range of 2.8–3.3 Å for medium NOEs and the H1′–H3 distances are within the range of 3.3–5.0 Å for weak NOEs [36] which are consistent with the transglycosidic NOE intensity pattern presented in Table 7 as $\mathbf{I}_{H1'-H4} \gg \mathbf{I}_{H1'-H5} > \mathbf{I}_{H1'-H3}$.

It can be said that the H1′–H4 distance of the primary neamine species becomes shorter upon deprotonation of the amino groups as pD increases, which brings about clockwise rotation about the glycosidic ϕ/ψ dihedral angles due possibly to varying electrostatic equilibrium between the amino groups at different pDs. For instance; H1′–H4/ϕ/ψ is 2.79(Å)/−41.5(°)/−56.6(°) for nea-4H and 2.39(Å)/−26.7(°)/−33.5(°) for nea-2H (Table 8). As seen in the best representative clustered neamine structures in Fig. 13A–C for nea-4H/3H/2H, respectively, the negative syn-ψ geometry is stabilized

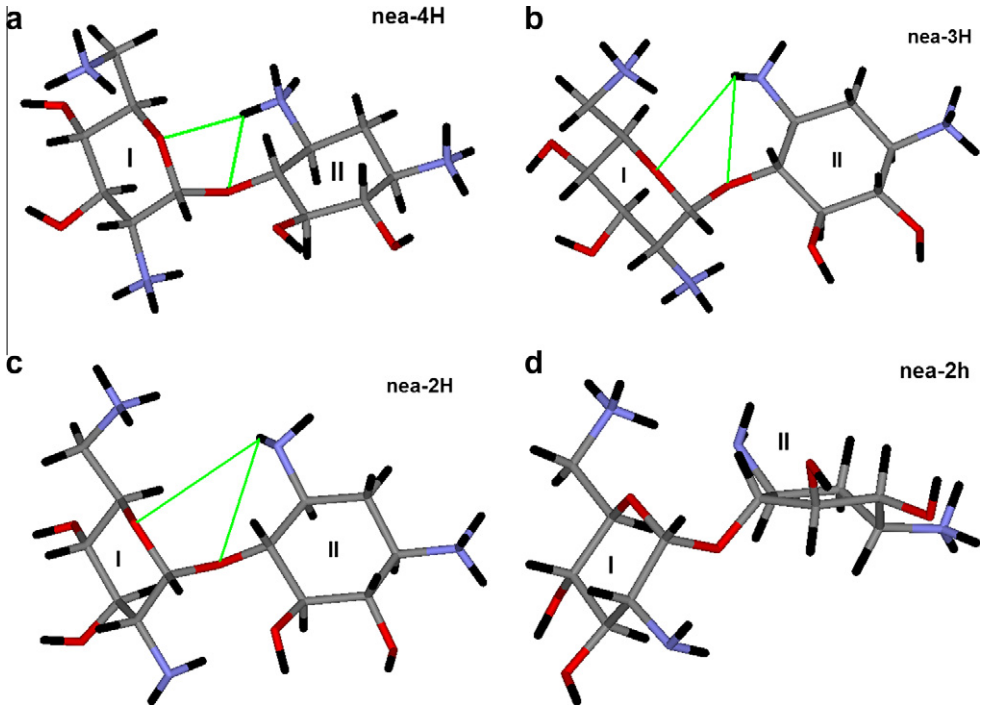

Fig. 13. Representative cluster structures of (A) nea-4H, (B) nea-3H, (C) nea-2H and (D) nea-2h, which are in good agreement with NMR data. Green lines represent inter-residual H-bonding interactions.

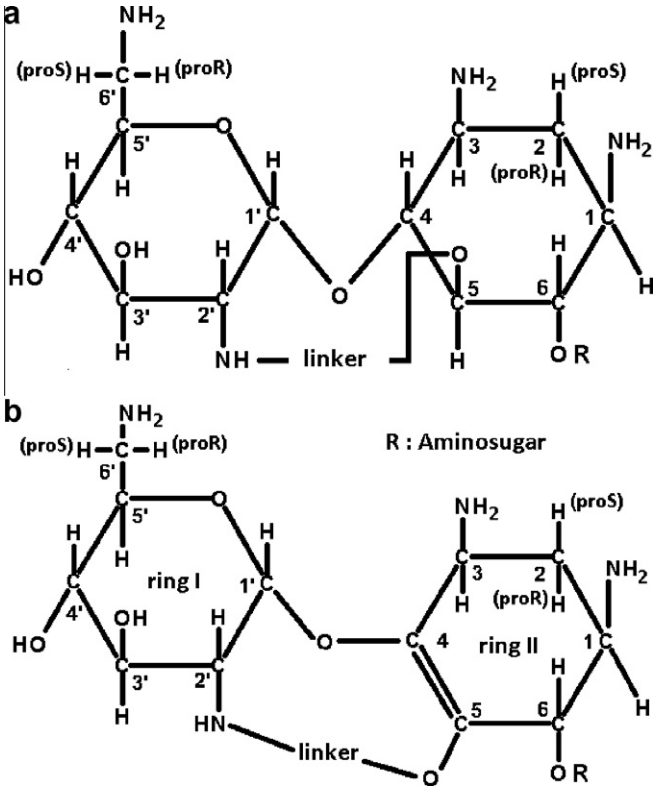

Fig. 14. Rational drug design for novel aminoglycosides. (A) Use of a linker between N2′ of ring I and O5 of ring II, and (B) introduction of a double-bond between C4 and C5 of ring II in addition to A.

by an inter-residual bifurcated H-bond from N3H of ring II to O5′ of ring I and the glycosidic O. Compared to the H1′–H4 distance nea-2H (2.398 Å), Table 8, the h1′–h4 distance of nea-2h (2.555 Å) is observed to increase by ~0.2 Å as a result of the ring II conversion from $^4C_1$ to $^6rH_1$. Such an increase is compensated by ϕ/ψ rotation by −27(°)/+19(°) about the glycosidic bonds of nea-2h. This in turn disrupts the expected inter-residual bifurcated H-bond in the secondary neamine species (Fig. 13D), which provides a more flexible attribution about the glycosidic bonds of the secondary neamine species, and yet stable enough to preserve the negative syn-ψ geometry in solution.

According to the Boltzmann distribution law results given in Table 8, nea-3H and nea-2H/h were found to adopt the gt exocyclic rotamer while nea-4H favors the gg exocyclic rotamer. It is highly likely that, when all amino groups are protonated, the electrostatic repulsions between $N6'H_3^+$ of ring I and $N3H_3^+$ of ring II forces the exocyclic group of ring I to adopt the gg rotamer orientation. Such an electrostatic tension is relieved when $N3H_2$ of ring II is not protonated, yielding the gt exocyclic rotamer orientation.

3.7. Rational drug design

Aminoglycoside modifying enzymes are able to surmount the energy barrier to convert the glycosidic syn-ψ geometry to anti-ψ geometry, which is the preferred conformation for the adenylation of kanamycin in the active site of ANT 4 [7]. To prevent the modification of kanamycin-like aminoglycoside antibiotics by ANT 4, Asensio et al. [6,8] synthesized a conformationally locked neomycin B to immobilize the glycosidic rotations between ring I and II. The locked neomycin B succeded to evade bacterial resistance, but exhibited lower binding affinity than neomycin B towards the A-site of 16S rRNA. In a similar vein to the locked aminoglycoside strategy, Fig. 14A, we computationally determined that an ethylmethylether tether placed between the N2′ atom of ring I and the O5 atom of ring II significantly enhances the binding affinity of locked kanamycin B-like aminoglycosides (data not shown).

It is highly likely that the existence of a half-chair conformer on ring II would facilitate the entropy of binding to the A-site of 16S

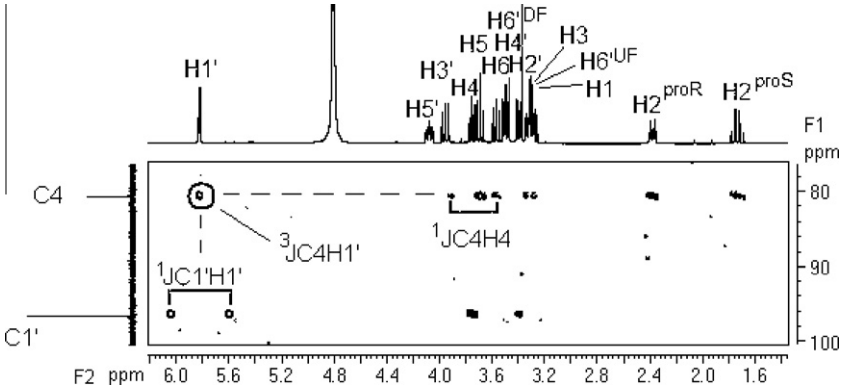

Fig. A1. An exemplary gHMBC spectrum showing the C4–H1′ transglycosidic connectivity for nea65p. This spectrum was obtained with a delay time of 1/2.jnxh (where jnxh = 10 Hz for three-bond correlations). A strong three-bond correlation between C4 and H1′) is circled at 5.82 ppm on F2 dimension with a dashed-line pointing to the C4–H4 cross-peak (split by $^{1}J_{C4-H4}$ ~140 Hz).

rRNA. Therefore it is proposed in this paper that the presence of a double-bond between C4 and C5 in a conformationally locked kanamycin B derivative, as exemplified in Fig. 14B, would mimic a half-chair conformer on ring II and ease-up the binding process by a more favorable entropy of binding.

Acknowledgment

We would like to thank the TR-Grid e-Infrastructure of Turkey for allowing us to use AMBER v10.

Appendix A

See Fig. A1.

Appendix B

See Fig. B1.

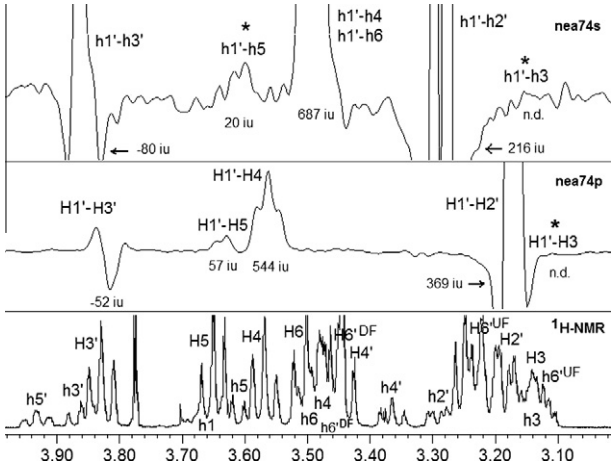

Fig. B1. Transglycosidic/anomeric NOE traces for nea74. The overlayed spectra show transglycosidic NOE traces for nea74s (top) and nea74p (middle) extracted from the corresponding 2D-NOESY spectrum acquired with a mixing time of 75 ms. The corresponding ^{1}H NMR spectrum is given at the bottom of the figure. "iu" values marked on the traces are transglycosidic integral units normalized to the corresponding reference diagonal peak (H1′ for the primary species and h1′ for the secondary species) measured on the 2D-NOESY spectrum. The reference diagonal peak was set to 100,000 iu. "*" = very low signal-to-noise ratio. "n.d." = not determined. The strongest transglycosidic NOE cross-peaks from h1′ to h4 (positioned at 3.47 ppm on F2 dimension with 687 positive integral units, top spectrum) and from H1′ to H4 (positioned at 3.57 ppm on F2 dimension with 544 positive integral units, middle spectrum) are clearly seen for nea74s and nea74p, respectively.

References

[1] T. Korzybski, Z. Kowszyk-Gindifer, W. Kurylowicz, Antibiotics, Origin Nature, and Properties, American society for microbiology, Washington DC, 1978.
[2] B.P. Rosen, S. Mobashery, Resolving the Antibiotic Paradox: Progress in Drug Design and Resistance, Plenum Press, New York, 1999.
[3] H.P. Rang, M.M. Dale, J.M. Ritter, P. Gardner, Pharmacology, Churchill Livingstone, 1995.
[4] H. Umezawa, I.R. Hooper, Aminoglycoside Antibiotics, Springer Verlag, New York, 1982.
[5] S.S. Hegde, F. Javid-Majd, J.S. Blanchard, J. Biol. Chem. 276 (2001) 45876–45881.
[6] A. Bastida, A. Hidalgo, J.L. Chiara, M. Torrado, F. Corzana, J.M. P-Canadillas, P. Groves, E. G-Junceda, C. Gonzalez, J. J-Barbero, J.L. Asensio, J. Am. Chem. Soc. 128 (2006) 100–116.
[7] L.C. Pedersen, M.M. Benning, H.M. Holden, Biochemistry 34 (1995) 13305–13311.
[8] J.L. Asensio, A. Hidalgo, A. Bastida, M. Torrado, F. Corzana, J.L. Chiara, E.G. Junceda, J. Cañada, J.J. Barbero, J. Am. Chem. Soc. 127 (2005) 8278–8279.
[9] D. Fourmy, M.I. Recht, S.C. Blanchard, J.D. Puglisi, Science 274 (1996) 1367–1371.
[10] Q. Vicens, E. Westhof, J. Mol. Biol. 326 (2003) 1175–1188.
[11] W.K.C. Park, M. Auer, H. Kaksche, C.-H. Wong, J. Am. Chem. Soc. 118 (1996) 10150–10155.
[12] W.A. Greenberg, E.S. Priestly, P.S. Sears, P.B. Alper, C. Rosenbohm, M. Hendrix, S.-C. Hung, C.-H. Wong, J. Am. Chem. Soc. 121 (1999) 6527–6541.
[13] R. Tona, R. Bertolini, J. Hunziker, Org. Lett. 2 (2000) 1693–1696.
[14] M.D. Reily, L.C. Robosky, M.L. Manning, A. Butler, J.D. Baker, R.T. Winters, J. Am. Chem. Soc. 128 (2006) 12360–12361.
[15] C.A.G. Haasnoot, F.A.A.M. De Leeuw, C. Altona, Tetrahedron 236 (1980) 2783–2793.
[16] D.A. Case, T.A. Darden, T.E. Cheatham III, C.L. Simmerling, J. Wang, R.E. Duke, R. Luo, M. Crowley, R.C. Walker, W. Zhang, K.M. Merz, B. Wang, S. Hayik, A. Roitberg, G. Seabra, I. Kolossváry, K.F. Wong, F. Paesani, J. Vanicek, X. Wu, S.R. Brozell, T. Steinbrecher, H. Gohlke, L. Yang, C. Tan, J. Mongan, V. Hornak, G. Cui, D.H. Mathews, M.G. Seetin, C. Sagui, V. Babin, P.A. Kollman, AMBER v10, University of California CA, San Francisco Press, 2008.
[17] H. Jónsson, G. Mills, K.W. Jacobsen, Classical and Quantum Dynamics in Condensed Phase Simulations, World Scientific, Singapore, 1998.
[18] G. Mills, H. Jónsson, Phys. Rev. Lett. 72 (1994) 1124–1127.
[19] S.L. Dixon, K.M. Merz Jr., J. Chem. Phys. 107 (1997) 879–893.
[20] J. Wang, W. Wang, P.A. Kollman, D.A. Case, J. Mol. Graph. Mod. 25 (2006) 247–260.
[21] V. Hornak, R. Abel, A. Okur, B. Strockbine, A. Roitberg, C. Simmerling, Proteins 65 (2006) 712–725.
[22] K.N. Kirschner, R.J. Woods, Proc. Natl. Acad. Sci. USA 98 (2001) 10541–10545.
[23] D. Eisenberg, D. Crothers, Physical Chemistry with Applications to the Life Sciences, Addison-Wesley, 1979.
[24] R.E. Botto, B. Coxon, J. Am. Chem. Soc. 105 (1983) 1021–1028.
[25] W. Lesniak, J.M. Laren, W.R. Harris, V.L. Pecoraro, J. Schacht, Carbohydr. Res. 338 (2003) 2853–2862.
[26] Sutrisno, Y. Baran, G.A. Lawrance, E.I. von Nagy-Felsobuki, Struct. Chem. 12 (2001) 189–195.
[27] J.L. Asensio, A. Hidalgo, I. Cuesto, C. González, J. Cañada, C. Vicent, J.L. Chiara, G. Cuevas, J. Jiménez-Barbero, Chem. Eur. J. 8 (2002) 5228–5240.
[28] K. Popov, H. Rönkkömäki, L.H.J. Lajunen, Pure Appl. Chem. 78 (2006) 663–675.
[29] Y.A. Puius, T.H. Stievater, T. Srikrishnan, Carbohydr. Res. 341 (2006) 2871–2875.
[30] B. Francois, R.J. Russell, J.B. Murray, F. Aboul-Ela, B. Masquida, Q. Vicens, E. Westhof, Nucl. Acids Res. 33 (2005) 5677–5690.
[31] D. Mikhailov, K.H. Mayo, I.R. Vlahov, T. Toida, A. Pervin, R.J. Linhardt, Biochem. J. 318 (1996) 93–102.

[32] A.R. Ionescu, A. Bérces, M.Z. Zgierski, D.M. Whitfield, T. Nukada, J. Phys. Chem. A 109 (2005) 8096–8105.
[33] D.J. States, R.A. Haberkorn, D.J. Rune, J. Magn. Reson. 48 (1982) 286–292.
[34] F. Corzana, I. Cuesta, F. Freire, J. Revuelta, M. Torrado, A. Bastida, J.J. -Barbero, J.L. Asensio, J. Am. Chem. Soc. 129 (2007) 2849–2865. Supporting Information.
[35] J. Dabrowski, T. Kožár, H. Grosskurth, N.E. Nifantiev, J. Am. Chem. Soc. 117 (1995) 5534–5539.
[36] P.R. Andrews, C.H. Chang, R.M. Cooke, D.J. Craik, A.J. Edwards, J. Feeney, J.T. Gerik, C.N. Hodge, J.W. Jaroszewski, H. Kessler, G.F. King, R. Konat, J. Mackay, L.K. Nicholson, S. Pavlopoulos, D.G. Reid, M.S. Searle, W. Schmitt, P.J. Sweeney, G. Wickham, NMR in Drug Design, CRC Press Inc., USA, 1996.

Glossary

NMR: Nuclear magnetic resonance
NEB: Nudged elastic band
TS: Transition state